

Vector Single-Source SIE for TE Scattering From Objects Embedded in Multilayers

Zekun Zhu, Xiaochao Zhou, and Shunchuan Yang

Paper submitted to the IEEE Transactions on Antennas and Propagation

Abstract—A single-source (SS) surface integral equation (SIE) for transverse electric (TE) scattering from objects embedded in multilayers is proposed in this paper. Through recursively applying the surface equivalence theorem from innermost to outermost boundaries, an equivalent model with surface current sources enforced on the outermost boundary of the original object can be obtained. By further incorporated with the differential surface admittance operator (DSAO), only the electric current density is required. In addition, an efficient singularity cancellation approach is proposed to accurately evaluate singular and nearly singular integrals in the new formulation. Compared with other SIEs, like the Poggio-Miller-Chan-Harrington-Wu-Tsai (PMCHWT) formulation and other dual sources (DSs) formulations with both electric and magnetic current densities required, only single surface equivalent electric current density is required to be enforced on the outermost boundary in the proposed formulation. It is found that the overall count of unknowns and memory consumption can be significantly reduced and the conditioning of the final system is much better compared with the PMCHWT formulation. As numerical results shown, only a very small fraction amount of unknowns, memory and CPU time, 18%~30% of unknowns, 5%~9% of memory and 55%~70% of CPU time of the PMCHWT formulation in our simulations, is possibly needed in the proposed formulation.

Index Terms—Multilayers, method of moment, single-source formulation, surface equivalence theorem, singularity cancellation, TE polarization

I. INTRODUCTION

THE two-dimensional transverse electric (TE) electromagnetic analysis exist in many practical engineering applications, especially for objects embedded in multilayers, like power cables [1], infinite long transmission line [2]. It is more involved than the scalar transverse magnetic (TM) problems since vector field equations are required [3].

The method of moment (MOM) is widely used to solve the TE scattering problems due to its unknowns only residing in source regions and much less count of unknowns is needed compared with the volumetric mesh based method, like the finite-difference time-domain (FDTD) method [4], the finite element method (FEM) [5]. One of the most commonly

used surface integral equation (SIE) is the Poggio-Miller-Chan-Harrington-Wu-Tsai (PMCHWT) formulation [6]. In this formulation, dual sources (DSs) including both electric and magnetic current densities are required on each interface of different homogeneous media. Then, several variations, like the combined tangential formulation (CTF) [7], the Muller formulation [8], MT-PMCHWT [9] and PMCHWT-CBFM [10], are proposed to improve matrix conditioning and efficiency. However, a large system equation and many two-region problems need to be solved simultaneously when a large number of interfaces is involved.

Single-source(SS) formulations are proposed to model complex composite objects to improve the efficiency. For example, a single-source surface-volume-surface (SS-SVS) formulation is proposed to solve the TE scattering problems of penetrable objects [11]. Through mapping the surface to volume integral operator and then back to the surface integral operator, it can significantly improve the efficiency compared with the volume integral equation (VIE). Other various SS-SIEs are proposed to model penetrable objects [12]–[15]. Since in those formulations only SS rather than DSs is required, they are more efficient than their DSs counterparts. In [16], a generalized impedance boundary condition (GIBC) is used to model interconnects through eliminating the magnetic current density. In addition, the differential surface admittance operator (DSAO) [17] with only single electric current density is proposed to model two-dimensional rectangular interconnects. Then, it is extended to model various shaped cables and interconnects [18]–[21], and to solve three-dimensional scattering problems [22], model antennas [23] [24], and composite lossy conductors [25] [26].

Besides those SS formulations, several equivalence principle algorithms (EPAs) [27] [28] with both electric and magnetic current densities are used to solve three-dimensional scattering problems. In [29], the EPA combined with the connection scheme is proposed to model periodic perfectly electric conductor (PEC) embedded in planar multilayer media for TM scattering. Through recursively applying the boundary condition at the interfaces between two different planar media, the scattering problem by the multilayer media can be efficiently solved. In those EPAs, both the electric and magnetic current densities are required on a closed surface due to Love's equivalence theorem [30]. However, when objects are fully embedded in multilayers, which are interested in this paper, all these formulations can not solve the problem or still suffer from the efficiency issue.

In this paper, a new vector SS-SIE is proposed to solve the

Manuscript received xxx; revised xxx.

This work was supported in part by the National Natural Science Foundation of China through Grant 61801010, in part by Beijing Natural Science Foundation through Grant 4194082, and in part by Fundamental Research Funds for the Central Universities. (*Corresponding author: Shunchuan Yang*)

Z. Zhu and X. Zhou are with the School of Electronic and Information Engineering, Beihang University, Beijing, 100083, China (e-mail: zekun-zhu@buaa.edu.cn, zhouxiaochao@buaa.edu.cn.)

S. Yang is with the Research Institute for Frontier Science and the School of Electronic and Information Engineering, Beihang University, Beijing, 100083, China (e-mail: scyang@buaa.edu.cn.)

TE scattering problems of objects embedded in multilayers as shown in Fig. 1(a). In the proposed formulation, the surface equivalence theorem [31] is recursively applied from the innermost to outermost boundaries, original objects are replaced by the background medium as shown in Fig. 1(b). Through incorporating with the differential surface admittance operator (DSAO) [17], only single electric current density is required to be enforced on the *outermost* boundary. In addition, if multiple repetitions within structures, like identical elements in a large array [23], exist, the equivalent surface current density can only be calculated once for each type of scatters. Therefore, it can further improve the efficiency. In addition, an efficient approach through combining the numerical integration and the analytical integration is proposed to accurately calculate singular and nearly singular integrals in the proposed formulation.

It should be noted that the proposed approach is different from those in [32], in which a recursive Green's function is constructed through recursively uniting fictitious cells. However, the proposed approach directly uses the surface equivalence theorem on each interface and derives the equivalent current density. Compared with the recursive blockwise inversion of the full matrix method [16], the proposed formulation has strictly physical interpretation rather than purely mathematical manipulations. This paper explores the possibility which the surface equivalence theorem solves vector scattering problems by objects embedded in multilayers and greatly extends our previous work [33] [34], which only solve the scalar TM scattering problems.

Compared with our previous work and existing literature, its contributions in this paper are twofold.

- 1) A new vector SS-SIE is proposed to solve the TE scattering problems by penetrable or PEC objects embedded in multilayers. In the proposed formulation, only single electric current density is required to be enforced on the *outermost* boundary of objects, which retains fields the same as those in the original problem. The proposed approach decomposes the original large two-region problem into several small scattering ones. Therefore, significant efficiency improvements in terms of CPU time and memory usage can be obtained.
- 2) An efficient singularity cancellation approach is proposed to handle various types of singular and nearly singular integrals in the proposed formulation. Through combining the numerical integration and the analytical integration, all the matrix elements can be accurately and efficiently calculated. Our numerical results show that the proposed approach can significantly improve the convergence rate and only uses less than ten integration points to reach the level of machine precision.

This paper is organized as follows. In Section II, the configurations and preliminaries are first demonstrated. Then, the surface equivalence theorem is briefly summarized to demonstrate the derivation of the SS formulation. The proposed SS-SIE formulation is detailed demonstrated to model a single penetrable object and then a penetrable or PEC object embedded in another medium. At last, extension of

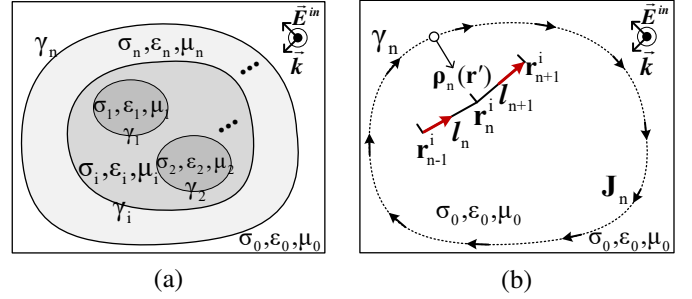


Fig. 1. (a) The TE scattering on objects embedded in multilayers, (b) the equivalent model with the electric current density enforced on the outermost boundary γ_n .

the proposed approach to model objects embedded into any multilayers is illustrated. In Section III, through combining the surface current density and the electric field integral equation (EFIE) on the outermost boundary, the proposed SS-SIE to solve the exterior scattering problem is presented. In Section IV, detailed formulations of the proposed singularity cancellation approach are demonstrated. In Section V, the accuracy of the proposed singularity cancellation approach and the performance of the proposed SS-SIE are comprehensively investigated through several numerical examples. At last, we draw some conclusions in Section VI.

II. METHODOLOGY

A. The Configurations and Preliminaries

The TE scattering on penetrable objects with arbitrary shapes embedded in multilayers is considered as shown in Fig. 1(a). The penetrable object with constant material parameters ϵ_i, σ_i and μ_i is enclosed by two adjacent enclosed boundaries γ_i . The background medium is air with constant material parameters ϵ_0, σ_0 and μ_0 . Each boundary is discretized with N_1, N_2, \dots, N_n line segments. A TE-polarized plane wave incidents from the exterior region. According to the surface equivalence theorem [31], the scattering fields can be regarded to be generated by surface electric and magnetic current densities on the boundary enclosing the objects. Since fields outside objects are interested in our study, fields inside objects in the equivalent problem can be *arbitrary*. Therefore, an equivalent model as shown in Fig. 1(b) with only the electric current density \mathbf{J}_n enforced on the outermost boundary can be obtained through carefully selecting *arbitrary* fields inside objects after the penetrable objects are replaced by the background medium. Before we move to detailed formulation derivation, some symbol notations used in this paper are introduced.

A bold character with both a superscript and a subscript, like $\mathbf{U}_{(i,j)}^k$, denotes a matrix, where the superscript represents that this matrix is related to the surface equivalence theorem applied for the k th time and the subscript (i, j) denotes the i th and j th boundaries are the source and testing ones, respectively. A bold character with only a subscript, like \mathbf{E}_i , denotes a vector defined on γ_i . A quantity with $\hat{\cdot}$, like $\hat{\mathbf{E}}$,

denotes that it is for the equivalent problem. The inner product of two vectors \mathbf{f} and \mathbf{g} is defined as

$$\langle \mathbf{f}(\mathbf{r}), \mathbf{g}(\mathbf{r}) \rangle = \int_{\gamma} \mathbf{f}(\mathbf{r}) \cdot \mathbf{g}(\mathbf{r}) dr. \quad (1)$$

B. The Surface Equivalence Theorem

According to the surface equivalence theorem [30], any enclosed boundary with surface electric and magnetic current densities can reproduce exactly the same fields in the equivalent configurations. The equivalent electric and magnetic current densities are expressed as

$$\widehat{\mathbf{J}}_i(\vec{r}) = \mathbf{H}_{t_i}(\vec{r}) - \widehat{\mathbf{H}}_{t_i}(\vec{r}), \quad (2)$$

$$\widehat{\mathbf{M}}_i(\vec{r}) = \mathbf{E}_{t_i}(\vec{r}) - \widehat{\mathbf{E}}_{t_i}(\vec{r}), \quad (3)$$

where $\vec{r} \in \gamma_i$, $\mathbf{E}_{t_i}(\vec{r})$, $\widehat{\mathbf{E}}_{t_i}(\vec{r})$, $\mathbf{H}_{t_i}(\vec{r})$, $\widehat{\mathbf{H}}_{t_i}(\vec{r})$ are the surface tangential electric and magnetic fields in the original and equivalent model, respectively. When $\widehat{\mathbf{E}}_{t_i}(\vec{r}) = \widehat{\mathbf{H}}_{t_i}(\vec{r}) = \mathbf{0}$, it corresponds to the Love's equivalence theorem. In this paper, we use other options to derive a SS formulation [17] [23].

One option to obtain the single electric current density formulation is to enforce $\mathbf{E}_{t_i}(\vec{r}) = \widehat{\mathbf{E}}_{t_i}(\vec{r})$. Then, (2) and (3) are rewritten as

$$\widehat{\mathbf{J}}_i(\vec{r}) \neq \mathbf{0}, \widehat{\mathbf{M}}_i(\vec{r}) = \mathbf{0}. \quad (4)$$

When $\mathbf{E}_{t_i}(\vec{r}) = \mathbf{0}$, (4) corresponds to PEC objects and $\mathbf{E}_{t_i}(\vec{r}) \neq \mathbf{0}$ for penetrable objects. Therefore, it is applicable for both the PEC and penetrable objects.

Another option to obtain the single magnetic current density formulation is to enforce that $\mathbf{H}_{t_i}(\vec{r}) = \widehat{\mathbf{H}}_{t_i}(\vec{r})$. Therefore, (2) and (3) are expressed as

$$\widehat{\mathbf{M}}_i(\vec{r}) \neq \mathbf{0}, \widehat{\mathbf{J}}_i(\vec{r}) = \mathbf{0}. \quad (5)$$

When $\mathbf{H}_{t_i}(\vec{r}) = \mathbf{0}$, (5) corresponds to perfect magnetic conductor (PMC) objects and $\mathbf{H}_{t_i}(\vec{r}) \neq \mathbf{0}$ for dielectric objects. Therefore, it is applicable for both the PMC and penetrable objects.

Both (4) and (5) allow us to derive a SS formulation. In this paper, (4) is used to derive the SS formulation by enforcing that all tangential electric fields inside γ_i in the original and equivalent problems equal to each other. It should be noted that fictitious fields are obtained inside the penetrable objects since the equivalent theorem is applied. If those fields are anyway required, they can be recovered through the surface electric current density.

C. The SS-SIE for A Penetrable Object Embedded in the Background Medium

A single penetrable object with constant parameters ε_1 , σ_1 , and μ_1 and the boundary γ_1 as shown in Fig. 2(a) is first considered. We reported the preliminary idea in [35]. Detailed formulations are presented in this subsection.

According to the Stratton-Chu formulation [31], the electric field \mathbf{E} inside γ_1 can be expressed as

$$T\hat{\mathbf{t}}(\mathbf{E}) = \hat{\mathbf{t}}(\mathcal{L}_1[\mathbf{n}' \times \mathbf{H}]) + \hat{\mathbf{t}}(\mathcal{K}_1[\mathbf{n}' \times \mathbf{E}]), \quad (6)$$

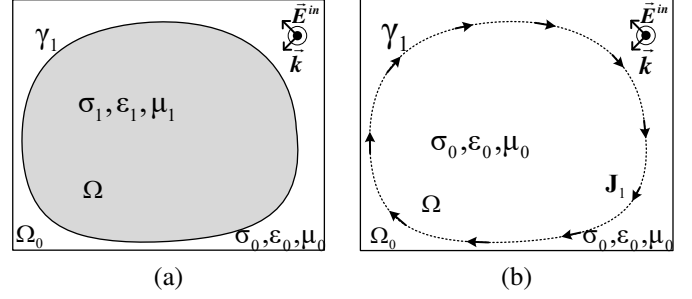


Fig. 2. (a) The TE scattering problem on a penetrable object, (b) the equivalent model with the electric current density enforced on γ_1 .

where

$$\hat{\mathbf{t}}(\mathbf{A}) = \mathbf{n} \times \mathbf{n} \times \mathbf{A}, \quad (7)$$

$$\mathcal{L}_1(\mathbf{A}) = -j\omega\mu \oint_{\gamma_1} \left(1 + \frac{1}{k_1^2} \nabla' \nabla' \cdot\right) G_1(\mathbf{r}, \mathbf{r}')(\mathbf{A}) d\mathbf{r}', \quad (8)$$

$$\mathcal{K}_1(\mathbf{A}) = \oint_{\gamma_1} (\mathbf{A}) \times \nabla' G_1(\mathbf{r}, \mathbf{r}') d\mathbf{r}', \quad (9)$$

\mathcal{K}_1 is Cauchy principal value without including the residual term. \mathbf{E} and \mathbf{H} are electric and magnetic fields inside γ_1 , \mathbf{n}' denotes a unit normal vector pointing to the interior region of γ_1 , the Green's function is $G_1(\mathbf{r}, \mathbf{r}') = -(j/4) H_0^{(2)}(k_1|\mathbf{r} - \mathbf{r}'|)$ inside the penetrable object, and $H_0^{(2)}(\cdot)$ is the zeroth order Hankel function of the second kind, $T = 1/2$ when \mathbf{r} and \mathbf{r}' are located on the same boundary, otherwise, $T = 1$.

The vector basis function $\mathbf{f}_n(\mathbf{r}')$ [3] and the dual vector basis function $\mathbf{n}' \times \mathbf{f}_n(\mathbf{r}')$ are used to expand $\mathbf{n}' \times \mathbf{H}$ and $\mathbf{n}' \times \mathbf{E}$. $\mathbf{f}_n(\mathbf{r}')$ is defined as

$$\mathbf{f}_n(\mathbf{r}') = \begin{cases} \frac{\mathbf{r}' - \mathbf{r}_{n-1}^i}{l_n}, & \mathbf{r}' \in [\mathbf{r}_{n-1}^i, \mathbf{r}_n^i] \\ \frac{\mathbf{r}_{n+1}^i - \mathbf{r}'}{l_{n+1}}, & \mathbf{r}' \in [\mathbf{r}_n^i, \mathbf{r}_{n+1}^i] \end{cases}, \quad (10)$$

where $\mathbf{f}_n(\mathbf{r}')$ is the n th basis function, l_n and l_{n+1} are the length of the n th and $(n+1)$ th segments and \mathbf{r}_{n-1}^i , \mathbf{r}_n^i , \mathbf{r}_{n+1}^i are the endpoints of the n th and $(n+1)$ th segments as shown in Fig. 1(b), respectively. $\mathbf{f}_n(\mathbf{r}')$ mimics the RWG basis function in three-dimensional space and is also divergence free [3]. Therefore, $\mathbf{n}' \times \mathbf{E}$ and $\mathbf{n}' \times \mathbf{H}$ can be expanded as

$$\mathbf{n}' \times \mathbf{E} = \sum e_1^n \mathbf{n}' \times \mathbf{f}_n(\mathbf{r}'), \quad (11)$$

$$\mathbf{n}' \times \mathbf{H} = \sum h_1^n \mathbf{f}_n(\mathbf{r}'). \quad (12)$$

$\mathbf{n}' \times \mathbf{E}$ is expanded through the dual vector basis function $\mathbf{n}' \times \mathbf{f}_n(\mathbf{r}')$ rather than $\mathbf{f}_n(\mathbf{r}')$ to well test the residual term on the left hand side (LHS) of (6) [36].

Then, $\mathbf{f}_n(\mathbf{r})$ is used to test (6) and we obtain

$$TU_{(1,1)}^1 \mathbf{E}_1 = \mathbf{L}_{(1,1)}^1 \mathbf{H}_1 + \mathbf{K}_{(1,1)}^1 \mathbf{E}_1, \quad (13)$$

where $\mathbf{U}_{(1,1)}^1$, $\mathbf{L}_{(1,1)}^1$ and $\mathbf{K}_{(1,1)}^1$ are square matrixes with dimension of $N_1 \times N_1$. \mathbf{E}_1 and \mathbf{H}_1 are two column vectors including the expansion coefficients defined as

$$\mathbf{E}_1 = [e_1^1, e_1^2, e_1^3, \dots, e_1^{N_1}]^T, \quad (14)$$

$$\mathbf{H}_1 = [h_1^1, h_1^2, h_1^3, \dots, h_1^{N_1}]^T. \quad (15)$$

The entities of matrixes $\mathbf{U}_{(1,1)}^1$, $\mathbf{L}_{(1,1)}^1$ and $\mathbf{K}_{(1,1)}^1$ are given by

$$[\mathbf{U}_{(1,1)}^1]_{mn} = -\langle \mathbf{f}_m, \hat{\mathbf{t}}(\mathbf{f}_n) \rangle, \quad (16)$$

$$[\mathbf{L}_{(1,1)}^1]_{mn} = -\langle \mathbf{f}_m, \hat{\mathbf{t}}(\mathcal{L}_1(\mathbf{f}_n)) \rangle, \quad (17)$$

$$[\mathbf{K}_{(1,1)}^1]_{mn} = -\langle \mathbf{f}_m, \hat{\mathbf{t}}(\mathcal{K}_1[\mathbf{n}' \times \mathbf{f}_n]) \rangle. \quad (18)$$

Accurate evaluation of the singular and nearly singular integrals in (17) and (18) is required to obtain reliable results when the source and testing segments are overlapped and near to each other. Our numerical experiments show that traditional singularity approaches in [37] [38] are not enough to obtain accurate results. To mitigate the problem, we proposed another singularity cancellation approach through combining the numerical and radial integration approaches to accurately and efficiently calculate singular and nearly singular integrals in (17) and (18). Detailed formulations are presented in Section IV.

By moving the second term on the right hand side (RHS) of (13) to its LHS and inverting the square coefficient matrix, we get

$$\mathbf{H}_1 = \underbrace{[\mathbf{L}_{(1,1)}^1]^{-1}[\mathbf{T}\mathbf{U}_{(1,1)}^1 - \mathbf{K}_{(1,1)}^1]}_{\mathbf{Y}_1} \mathbf{E}_1, \quad (19)$$

where \mathbf{Y}_1 is the surface admittance operator (SAO) [17] for the original problem.

After the surface equivalence theorem [31] is applied, the penetrable object is replaced by its surrounding medium and surface equivalent current density is introduced to ensure fields in the exterior region unchanged as shown in Fig. 2(b). With similar procedure above, we obtain

$$\hat{\mathbf{H}}_1 = \underbrace{[\hat{\mathbf{L}}_{(1,1)}^1]^{-1}[\mathbf{T}\hat{\mathbf{U}}_{(1,1)}^1 - \hat{\mathbf{K}}_{(1,1)}^1]}_{\hat{\mathbf{Y}}_1} \mathbf{E}_1, \quad (20)$$

where $\hat{\mathbf{Y}}_1$ is the SAO [17] for the equivalent problem and all the material parameters are replaced by those of the surrounding medium.

Therefore, according to (4), the surface equivalent electric current density can be expressed as

$$\mathbf{J}_1 = \mathbf{H}_1 - \hat{\mathbf{H}}_1 = \underbrace{(\mathbf{Y}_1 - \hat{\mathbf{Y}}_1)}_{\mathbf{Y}_{\gamma_1}} \mathbf{E}_1, \quad (21)$$

where \mathbf{J}_1 is the expansion coefficients stored in a column vector when the equivalent current density on γ_1 is expanded by $\mathbf{f}_n(\mathbf{r}')$ and \mathbf{Y}_{γ_1} is the DSAO [17]. Magnetic current density is not required since we keep electric fields on the inner side of γ_1 in the original and equivalent problems unchanged as shown in (4).

D. The SS-SIE for A Two-layered Object Embedded in the Background Medium

Two scenarios, in which a dielectric or PEC object is embedded in the innermost region as shown in Fig. 3(a) and

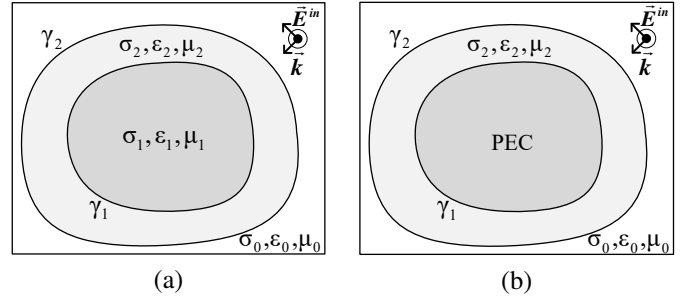


Fig. 3. (a) A two-layered penetrable object is embedded in the background region, (b) a penetrable object with a PEC object inside is embedded in the background region.

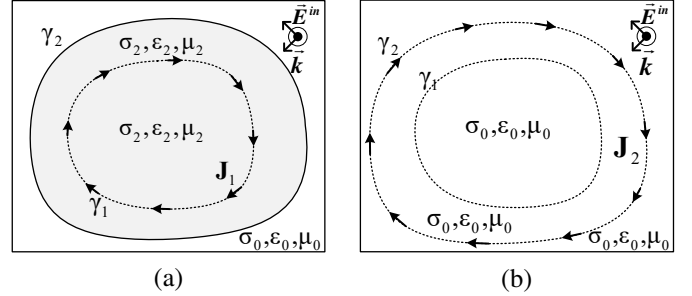


Fig. 4. (a) The TE scattering problem upon object embedded in a two-layered medium and the innermost penetrable object replaced by an equivalent current density, (b) the equivalent model in which the object is replaced by the background medium and only an equivalent electric current density enforced on γ_2 .

(b), are considered in this subsection. Our goal is to derive a surface equivalent electric current density \mathbf{J}_2 enforced on the outermost boundary γ_2 through recursively applying the surface equivalence theorem from γ_1 to γ_2 .

1) *A Dielectric Object in the Innermost Region:* Let's consider a dielectric object in the innermost region embedded into another medium in this subsection as shown in Fig. 3(a). After the inner penetrable object inside γ_1 is modeled through the approach presented in Section III-C, a surface equivalent current density \mathbf{J}_1 is obtained and enforced on γ_1 as shown in Fig. 4(a). Compared the equivalent model in Fig. 4(a) with that in Fig. 3(a), an equivalent current density \mathbf{J}_1 is enforced on γ_1 .

Then, the electric field inside γ_2 can be expressed through the Stratton-Chu formulation [31] as

$$\mathbf{T}\hat{\mathbf{t}}(\mathbf{E}) = \hat{\mathbf{t}}(\mathcal{L}[\mathbf{n}' \times \mathbf{H}]) + \hat{\mathbf{t}}(\mathcal{K}[\mathbf{n}' \times \mathbf{E}]) + \hat{\mathbf{t}}[\mathbf{L}(\mathbf{J}_1)]. \quad (22)$$

The tangential magnetic field $\mathbf{n}' \times \mathbf{H}$ and the electric current density \mathbf{J}_1 are expanded by $\mathbf{f}_n(\mathbf{r}')$ and the tangential electric field $\mathbf{n}' \times \mathbf{E}$ is expanded by $\mathbf{f}_n(\mathbf{r}')$. $\mathbf{f}_n(\mathbf{r}')$ is used to test (22) on γ_1 . The following matrix equation is obtained

$$\mathbf{T}\mathbf{U}_{(1,1)}^2 \mathbf{E}_1 = \mathbf{L}_{(2,1)}^2 \mathbf{H}_2 + \mathbf{K}_{(2,1)}^2 \mathbf{E}_2 + \mathbf{L}_{(1,1)}^2 \mathbf{J}_1, \quad (23)$$

where $\mathbf{U}_{(1,1)}^2$, $\mathbf{L}_{(2,1)}^2$, $\mathbf{K}_{(2,1)}^2$, and $\mathbf{L}_{(1,1)}^2$ are matrixes with dimension of $N_1 \times N_1$, $N_1 \times N_2$, $N_1 \times N_2$, and $N_1 \times N_1$. \mathbf{J}_1 , \mathbf{E}_2 , \mathbf{H}_2 denote the coefficient column vectors of the current density on γ_1 and tangential electric and magnetic fields on γ_2 , respectively. The entities of the above four matrixes are

calculated by

$$[\mathbf{U}_{(1,1)}^2]_{mn} = -\langle \mathbf{f}_m, \hat{\mathbf{t}}(\mathbf{f}_n) \rangle, \quad (24)$$

$$[\mathbf{L}_{(2,1)}^2]_{mn} = -\langle \mathbf{f}_m, \hat{\mathbf{t}}(\mathcal{L}_2(\mathbf{f}_n)) \rangle, \quad (25)$$

$$[\mathbf{K}_{(2,1)}^2]_{mn} = -\langle \mathbf{f}_m, \hat{\mathbf{t}}(\mathcal{K}_2[\mathbf{n}' \times \mathbf{f}_n]) \rangle, \quad (26)$$

$$[\mathbf{L}_{(1,1)}^2]_{mn} = -\langle \mathbf{f}_m, \hat{\mathbf{t}}(\mathcal{L}_2(\mathbf{f}_n)) \rangle. \quad (27)$$

By substituting (21) into (23), moving the last term on the RHS of (23) to its LSH and then inverting the square coefficient matrix, we obtain

$$\mathbf{E}_1 = \underbrace{[T\mathbf{U}_{(1,1)}^2 - \mathbf{L}_{(1,1)}^2 \mathbf{Y}_{\gamma_1}]^{-1}}_{\mathbf{C}_{\gamma_1}} [\mathbf{L}_{(2,1)}^2 \mathbf{H}_2 + \mathbf{K}_{(2,1)}^2 \mathbf{E}_2]. \quad (28)$$

By using $\mathbf{f}_n(\mathbf{r}')$ to test (22) on γ_2 , we have

$$T\mathbf{U}_{(2,2)}^2 \mathbf{E}_2 = \mathbf{L}_{(2,2)}^2 \mathbf{H}_2 + \mathbf{K}_{(2,2)}^2 \mathbf{E}_2 + \mathbf{L}_{(1,2)}^2 \mathbf{J}_1, \quad (29)$$

where $\mathbf{U}_{(2,2)}^2$, $\mathbf{L}_{(2,2)}^2$, $\mathbf{K}_{(2,2)}^2$, and $\mathbf{L}_{(1,2)}^2$ are matrixes with dimension of $N_2 \times N_2$, $N_2 \times N_2$, $N_2 \times N_2$, and $N_2 \times N_1$. Their entities are similar to $\mathbf{U}_{(1,1)}^2$, $\mathbf{L}_{(2,1)}^2$, $\mathbf{K}_{(2,1)}^2$, and $\mathbf{L}_{(1,1)}^2$ and can be calculated by (24)-(27).

By substituting (21) and (28) into (29) and rearranging each term, the relationship between the tangential electric and magnetic field on γ_2 can be expressed as

$$\mathbf{H}_2 = \mathbf{Y}_2 \mathbf{E}_2, \quad (30)$$

where

$$\mathbf{Y}_2 = \left[\mathbf{L}_{(2,2)}^2 + \mathbf{L}_{(1,2)}^2 \mathbf{Y}_{\gamma_1} \mathbf{C}_{\gamma_1} \mathbf{L}_{(2,1)}^2 \right]^{-1} \cdot \left[T\mathbf{U}_{(2,2)}^2 - \mathbf{K}_{(2,2)}^2 - \mathbf{L}_{(1,2)}^2 \mathbf{Y}_{\gamma_1} \mathbf{C}_{\gamma_1} \mathbf{K}_{(2,1)}^2 \right]. \quad (31)$$

2) *A PEC Object in the Innermost Region:* When the innermost embedded object is PEC, \mathbf{J}_1 physically exists and tangential electric fields vanish on γ_1 . Therefore, \mathbf{E}_1 equals to zero on the LHS of (23) and we get

$$\mathbf{0} = \mathbf{L}_{(2,1)}^2 \mathbf{H}_2 + \mathbf{K}_{(2,1)}^2 \mathbf{E}_2 + \mathbf{L}_{(1,1)}^2 \mathbf{J}_1. \quad (32)$$

By inverting square matrix $\mathbf{L}_{(1,1)}^2$, we get

$$\mathbf{J}_1 = -\left[\mathbf{L}_{(1,1)}^2 \right]^{-1} \left[\mathbf{L}_{(2,1)}^2 \mathbf{H}_2 + \mathbf{K}_{(2,1)}^2 \mathbf{E}_2 \right]. \quad (33)$$

Then, after substituting (33) into (29) and rearranging each term, we have

$$\mathbf{H}_2 = \mathbf{Y}_{\text{PEC}} \mathbf{E}_2, \quad (34)$$

where

$$\mathbf{Y}_{\text{PEC}} = \left[\mathbf{L}_{(2,2)}^2 - \mathbf{L}_{(1,2)}^2 [\mathbf{L}_{(1,2)}^2]^{-1} \mathbf{L}_{(2,1)}^2 \right]^{-1} \left[T\mathbf{U}_{(2,2)}^2 - \mathbf{K}_{(2,2)}^2 - \mathbf{L}_{(1,2)}^2 [\mathbf{L}_{(1,2)}^2]^{-1} \mathbf{K}_{(2,1)}^2 \right]. \quad (35)$$

3) *Equivalent Problem:* After the surface equivalence theorem is applied on γ_2 , the object is replaced by the background medium and there is no current source inside γ_2 as shown in Fig. 4(b). With the similar procedure in the previous

subsection, we obtain

$$\hat{\mathbf{H}}_2 = \underbrace{[\hat{\mathbf{L}}_{(2,2)}^2]^{-1} [T\hat{\mathbf{U}}_{(2,2)}^2 - \hat{\mathbf{K}}_{(2,2)}^2]}_{\hat{\mathbf{Y}}_2} \mathbf{E}_2, \quad (36)$$

where the entities of matrix $\hat{\mathbf{L}}_{(2,2)}^2$, $\hat{\mathbf{U}}_{(2,2)}^2$ and $\hat{\mathbf{K}}_{(2,2)}^2$ are given by

$$[\hat{\mathbf{U}}_{(2,2)}^2]_{mn} = -\langle \mathbf{f}_m, \hat{\mathbf{t}}(\mathbf{f}_n) \rangle, \quad (37)$$

$$[\hat{\mathbf{L}}_{(2,2)}^2]_{mn} = -\langle \mathbf{f}_m, \hat{\mathbf{t}}(\mathcal{L}_0(\mathbf{f}_n)) \rangle, \quad (38)$$

$$[\hat{\mathbf{K}}_{(2,2)}^2]_{mn} = -\langle \mathbf{f}_m, \hat{\mathbf{t}}(\mathcal{K}_0[\mathbf{n}' \times \mathbf{f}_n]) \rangle. \quad (39)$$

Then, (34) for penetrable objects or (30) for PEC objects can be substituted into (4). Therefore, the surface equivalent electric current density \mathbf{J}_2 on γ_2 can be expressed as

$$\mathbf{J}_2 = \mathbf{H}_2 - \hat{\mathbf{H}}_2 = \underbrace{(\mathbf{Y}_{2/\text{PEC}} - \hat{\mathbf{Y}}_2)}_{\mathbf{Y}_{\gamma_2}} \mathbf{E}_2, \quad (40)$$

\mathbf{Y}_{γ_2} is the DSAO on γ_2 , which relates the tangential electric field to surface equivalence current density.

Compared with the micromodeling approach proposed in [34] for antenna array modeling, which is only applicable for the PEC object embedded in the background medium, the approach in this paper is applicable for much more general scenarios including both penetrable and PEC objects. In addition, as shown in the later subsection, the proposed approach is still suitable for objects embedded in multilayers. Therefore, the micromodeling approach in [34] can be regarded as a special case proposed in this paper.

E. Extension of the Proposed Formulation for Objects Embedded in Multilayers

For objects embedded in multilayers, the TE scattering fields caused by objects can be still equivalent to the scattering fields generated by a single electric current density on the outermost boundary γ_n . To generalize the proposed approach for such objects, the surface equivalence theorem is recursively applied from γ_1 to γ_n . Eventually, the equivalent current density \mathbf{J}_n on γ_n can be obtained. The procedure is similar to that in the previous subsection. Then, we get

$$\mathbf{J}_n = \mathbf{Y}_{\gamma_n} \mathbf{E}_n, \quad (41)$$

where \mathbf{Y}_{γ_n} is the DASO on γ_n , which relates the tangential electric field to surface equivalence current density on γ_n .

When multiple scatters embedded in another medium, a block-diagonal operator \mathbf{Y}_{γ_i} is obtained from assembling each block DSAO [34].

III. SCATTERING MODELING OF THE PROPOSED SS-SIE

Once the equivalent current density \mathbf{J}_n on γ_n is derived through (41), the scattering problem shown in Fig. 1 can be solved by combining the EFIE. The electric field \mathbf{E} in the exterior region of γ_n is the superposition of the incident field \mathbf{E}^{inc} and the scattered field. Since the surface equivalent

current density \mathbf{J}_n exists on γ_n , the total electric field is expressed as

$$\mathbf{E}(\vec{r}) = -j\omega\mu \int_{\gamma_n} \mathbf{J}_n(\vec{r}') G_0(\vec{r}, \vec{r}') ds' + \mathbf{E}^{inc}, \quad (42)$$

where \vec{r}' on the outermost boundary γ_n of the object, G_0 is the Green's function expressed as $G_0 = -jH_0^{(2)}(k_0\rho)/4$, where k_0 is the wavenumber in the background medium. \mathbf{J}_n is the equivalent current density on γ_n . Through taking the observation points on γ_n and expanding the tangential electric fields with the dual vector basis function and the electric current density \mathbf{J}_n through the vector basis function, we have

$$\mathbf{U}_{(n,n)}^n \mathbf{E}_n = \mathbf{L}_{(n,n)}^n \mathbf{Y}_{\gamma_n} \mathbf{E}_n + \mathbf{E}^i. \quad (43)$$

The entities of in \mathbf{E}^i , $\mathbf{U}_{(n,n)}^n$ and $\mathbf{L}_{(n,n)}^n$ are expressed as

$$[\mathbf{E}^i]_m = -\langle \mathbf{f}_m, \hat{\mathbf{t}}(\mathbf{E}^{inc}) \rangle, \quad (44)$$

$$[\mathbf{U}_{(n,n)}^n]_{mn} = -\langle \mathbf{f}_m, \mathbf{f}_n \rangle, \quad (45)$$

$$[\mathbf{L}_{(n,n)}^n]_{mn} = -\langle \mathbf{f}_m, \hat{\mathbf{t}}(\mathcal{L}_0(\mathbf{f}_n)) \rangle. \quad (46)$$

Therefore, the scattering problem can be solved and \mathbf{E}_n on γ_n is expressed as

$$\mathbf{E}_n = \left[\mathbf{U}_{(n,n)}^n - \mathbf{L}_{(n,n)}^n \mathbf{Y}_{\gamma_n} \right]^{-1} \mathbf{E}^i. \quad (47)$$

IV. THE PROPOSED APPROACH FOR ACCURATE CALCULATION OF SINGULAR AND NEARLY SINGULAR INTEGRALS

In this paper, we proposed an accurate approach to calculate the nearly singular and singular integrals through combing the numerical and analytical integration approaches. The Green's function in the two dimensional space is the *zeroth* order Hankel's function of the second kind. When the source point \mathbf{r}' is close to the observation point \mathbf{r} , the Green's function has a $\ln R$ singularity. For the gradient of the Green's function, $\nabla'G(\mathbf{r}, \mathbf{r}')$, $1/R$ singularity exists. Therefore, when \mathbf{r} is close to \mathbf{r}' , the Green's function and its gradient show strong singular and nearly singular behaviors.

Two integrals shown in (8) and (9) are required in the proposed formulation. Two different scenarios are considered according to the augments as follows.

- 1) When $|k\mathbf{R}| = |k(\mathbf{r} - \mathbf{r}')| \geq 0.1$, direct numerical integration is used to evaluate (8) and (9) in the proposed formulation.
- 2) When $|k\mathbf{R}| = |k(\mathbf{r} - \mathbf{r}')| \leq 0.1$, small-argument approximation is used and the analytical approach to calculate Green's function and its gradient to ensure the accuracy.

With the small-argument approximation, the Green's function and its gradient can be expressed as,

$$G(|k\mathbf{R}|) \approx -\frac{j}{4} \left[1 - j\frac{2}{\pi} \ln \left(\frac{\gamma|k\mathbf{R}|}{2} \right) \right] \quad |\mathbf{R}| \rightarrow 0, \quad (48)$$

$$\nabla'G(|k\mathbf{R}|) \approx -\frac{j}{4} \left(\frac{k^2}{2} + \frac{2j}{\pi|\mathbf{R}|^2} \right) \mathbf{R} \quad |\mathbf{R}| \rightarrow 0, \quad (49)$$

where $\gamma = 1.781$.

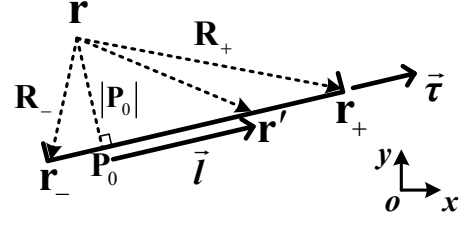


Fig. 5. The configuration of a test point and a source segment, where $\mathbf{R}_- = \mathbf{r} - \mathbf{r}_-$, $\mathbf{R}_+ = \mathbf{r} - \mathbf{r}_+$, $\mathbf{R} = \mathbf{r} - \mathbf{r}'$, $\vec{\tau} = \frac{\mathbf{r}_+ - \mathbf{r}_-}{|\mathbf{r}_+ - \mathbf{r}_-|}$, $|\mathbf{P}_0| = |\mathbf{P}_0 - \mathbf{r}|$, $l_- = \mathbf{R}_- \cdot \vec{\tau}$, $l_+ = \mathbf{R}_+ \cdot \vec{\tau}$, $\vec{l} = \vec{\tau}(\mathbf{R} \cdot \vec{\tau})$.

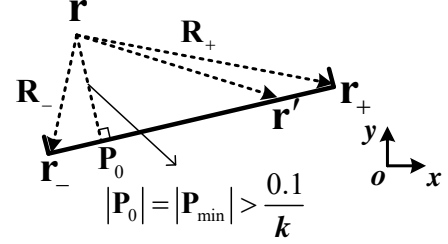


Fig. 6. No small argument approximation is used.

The outer integral of the double line integral in (7) and (8) is calculated through the five point Gaussian numerical integration. Careful attention should be paid to accurate evaluation of their inner integrals. Here, we consider a testing point \mathbf{r} and the inner integral segment l_i as shown in Fig. 5. \mathbf{p}_- and \mathbf{p}_+ are the endpoints of the source segment, \mathbf{r}' is a point on l_i and \mathbf{p}_0 is the projecting point from the observation point \mathbf{r} to l_i . Several other quantities are defined as shown in Fig. 5.

There are three scenarios for different distance between \mathbf{r} and l_i . First, the small argument is not applicable to evaluate the Green's function and its gradient as shown in Fig. 6. Second, the small argument should be used in the whole l_i as shown in Fig. 6. Third, only partial l_i is applicable for analytical evaluation of the Green's function and its gradient evaluation as shown in Fig. 8. Let $|\mathbf{P}_{min}| = \min(|\mathbf{R}_-|, |\mathbf{R}_+|, |\mathbf{P}_0|)$, $|\mathbf{P}_{max}| = \max(|\mathbf{R}_-|, |\mathbf{R}_+|, |\mathbf{P}_0|)$. Then, we presented the proposed efficiently approach for the singular and nearly singular integral evaluation.

A. No small argument approximation is used.

When $|k\mathbf{P}_{min}| \geq 0.1$ as shown in Fig. 6, the Green's function and its gradient can be accurately calculated through the recursive relationship of Hankel function [3]. Therefore, Gaussian numerical integration is used to calculate (8) and (9), five points Gaussian numerical integration is enough to obtain accurate results.

B. The small argument approximation is used in the whole l_i

When $|k\mathbf{P}_{max}| \leq 0.1$ as shown in Fig. 7, small arguments are used to approximate the Hankel function and its gradient. We proposed the following analytical approach to evaluate the inner integral of (8) and (9).

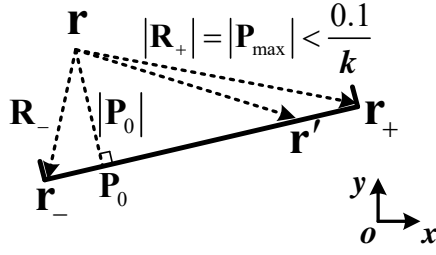


Fig. 7. The small argument approximation is used in the whole l_i .

According to (48), when the vector and dual vector basis functions are used to expand the tangential electric and magnetic fields, the analytical results of the operator $\mathcal{L}(\mathbf{A})$ can be evaluated with small-argument approximation as follows,

$$\begin{aligned} & \mathbf{f}_m(\mathbf{r}) \cdot \int_{l_n} \mathcal{L}[\mathbf{f}_n(\mathbf{r}')] \, d\mathbf{r}' \\ &= \frac{\omega\mu}{4} \left\{ \mathbf{f}_m(\mathbf{r}) \cdot \int_{l_n} \mathbf{f}_n(\mathbf{r}') G(k|\mathbf{P}|) \, d\mathbf{r}' - \right. \\ & \quad \left. \nabla \cdot \mathbf{f}_m(\mathbf{r}) \cdot \int_{l_n} \nabla' \cdot \mathbf{f}_n(\mathbf{r}') G(k|\mathbf{P}|) \, d\mathbf{r}' \right\} \\ &= c_0 \left\{ \mathbf{f}_m(\mathbf{r}) \cdot [I_7 + c_1 I_2 + (\mathbf{p}_0 - \mathbf{r}_{n-1}^i) \cdot (I_1 + I_6)] - \right. \\ & \quad \left. \nabla \cdot \mathbf{f}_m(\mathbf{r}) \cdot (\mathbf{r}) (I_6 + c_1 I_1) \right\}. \end{aligned} \quad (50)$$

Similarly, according to (49), the analytical results of the operator $\mathcal{K}(\mathbf{A})$ is calculated as follows,

$$\begin{aligned} & \mathbf{f}_m(\mathbf{r}) \cdot \int_{l_n} \mathcal{K}[\mathbf{n}' \times \mathbf{f}_n(\mathbf{r}')] \, d\mathbf{r}' \\ &= \frac{j}{4} \mathbf{f}_m(\mathbf{r}) \cdot \int_{l_n} [\mathbf{n}' \times \mathbf{f}_n(\mathbf{r}')] \times \nabla' G(k|\mathbf{P}|) \, d\mathbf{r}' \\ &= c_2 \mathbf{f}_m(\mathbf{r}) \cdot \{ \mathbf{v}_1 \times (c_3 I_7 + c_4 I_4) + \mathbf{v}_2 (c_3 I_6 + c_4 I_3) - \\ & \quad \mathbf{n}' (c_3 I_8 + c_4 I_5) + |\mathbf{p}_0| (c_3 I_7 + c_4 I_4) \} \end{aligned} \quad (51)$$

and c_0, c_1, c_2, c_3, c_4 are all constants and $\mathbf{v}_1, \mathbf{v}_2$ are constant vectors defined as,

$$c_0 = \frac{\omega\mu}{4l_{n(n+1)}}, \quad c_1 = -\frac{2j}{\pi} \ln(\gamma k/2), \quad (52)$$

$$c_2 = \frac{j}{4l_{n(n+1)}}, \quad c_3 = \frac{k^2}{2}, \quad c_4 = 2j/\pi,$$

$$\mathbf{v}_1 = \mathbf{n}' \times (\mathbf{p}_0 - \mathbf{r}_{n-1(n+1)}^i), \quad (53)$$

$$\mathbf{v}_2 = [\mathbf{n}' \times (\mathbf{p}_0 - \mathbf{r}_{n-1(n+1)}^i)] \times (\mathbf{p}_0 - \mathbf{r}),$$

where $l_{n(n+1)}$ and $\mathbf{r}_{n-1(n+1)}^i$ denote that when the first part of the basis function $\mathbf{f}_n(\mathbf{r}')$ is selected, l_n and \mathbf{r}_{n-1}^i are used, otherwise, l_{n+1} and \mathbf{r}_{n+1}^i should be used.

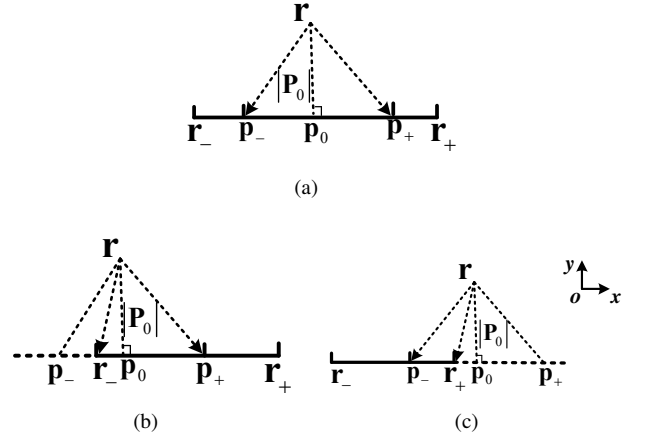


Fig. 8. The minimum value for $|\mathbf{R}|$ is $|\mathbf{p}_0|$, $|\mathbf{R}_-|$ or $|\mathbf{R}_+|$ in the case of (a), (b) or (c), respectively.

C. The small argument approximation is partially used on l_i .

When $|k\mathbf{P}_{min}| \leq 0.1$ and $|k\mathbf{P}_{max}| \geq 0.1$, there are three cases shown in Fig. 8. There may be two intersection points, \mathbf{r}_- and \mathbf{r}_+ in Fig. 8(a) and only one intersection point in Fig. 8(b) and Fig. 8(c). Therefore, it is found that (8) and (9) are divided into three cases as shown in Fig. 8.

- 1) When $|k\mathbf{P}_0| \leq 0.1$, $|k\mathbf{R}_-| \geq 0.1$ and $|k\mathbf{R}_+| \geq 0.1$ as shown in Fig. 8(a), the integral result of the whole segment may be divided into three parts, where the numerical integral is used for the intervals $[\mathbf{r}_-, \mathbf{p}_-]$, $[\mathbf{p}_+, \mathbf{r}_+]$ and the analytic method should be applied for the interval $[\mathbf{p}_-, \mathbf{p}_+]$.
- 2) When $|k\mathbf{R}_-| \leq 0.1$ and $|k\mathbf{R}_+| \geq 0.1$ as shown in Fig. 8(b), the source segment is divided into two parts, $[\mathbf{r}_-, \mathbf{p}_+]$ and $[\mathbf{p}_+, \mathbf{r}_+]$. Therefore, the inner line integration of (8) and (9) includes analytical integration in $[\mathbf{r}_-, \mathbf{p}_+]$ and numerical integration in $[\mathbf{p}_+, \mathbf{r}_+]$.
- 3) Fig. 8(c) is similar to Fig. 8(b), where $|k\mathbf{R}_-| \geq 0.1$ and $|k\mathbf{R}_+| \leq 0.1$.

In the proposed approach, the inner line integral can be accurately calculated and the outer line integral is calculated through the numerical integration. Through carefully considering the position of the source and testing segments as stated above, extremely fast convergence rate can be obtained. As shown in our numerical results, less than ten Gaussian integration points can reach the level of machine precision. Furthermore, the proposed approach can be easy to be used to evaluate different singular and nearly singular integrals from formulations, like in [39] [40].

V. NUMERICAL RESULTS AND DISCUSSION

Two numerical examples are first carried out to verify the convergence of the proposed singularity cancellation approach proposed in Section IV. Then, three TE-polarization scattering problems are solved to demonstrate the performance of the proposed SS-SIE.

The workstation with Intel i7-9750H 2.6 GHz CPU and 16G memory is used for all the experiments in this section. Our in-house codes are implemented in Matlab and full vectorization

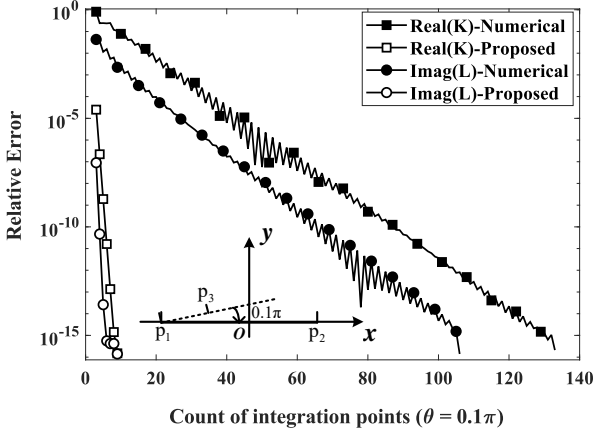


Fig. 9. Relative error obtained from the proposed approach and the fully numerical integration approach with $\theta = 0.1\pi$. The end points on source segment \mathbf{p}_1 , \mathbf{p}_2 are $(-0.065, 0, 0)$ [m] and $(0.065, 0, 0)$ [m], respectively. The testing point \mathbf{p}_3 is $(-0.046, 0.006, 0)$ [m] and 0.02 m away from \mathbf{p}_1 . The angle θ between the testing segment and source segments is 0.1π .

is explored to speed up the performance. Only a single thread is used for fair comparison.

A. Validation of the Proposed Singularity Cancellation Approach

Assuming the source and testing segments are located in the free space and then we calculated one element of matrixes \mathbf{L} and \mathbf{K} with a testing point and a source segment with two end points of $(-0.065, 0, 0)$ [m] and $(0.065, 0, 0)$ [m]. The frequency used in our simulations is 300 MHz. Two challenging scenarios are considered to validate the effectiveness of the proposed singularity cancellation approach. First, the testing segment is connected to the source segment at $(-0.065, 0, 0)$ [m]. One point, which is 0.02 m away from $(-0.065, 0, 0)$ [m] on the testing segment, is selected as the testing point. Then, the integration is calculated with rotating the testing segment in the counterclockwise direction at the common vertex from $\theta = 0.1\pi$ to π . In this configuration, the source segment is divided into two parts. One part satisfies the small argument approximation condition $|k\mathbf{R}| = |k(\mathbf{r} - \mathbf{r}')| \leq 0.1$. Therefore, the integration on this part are computed through the analytical formulations in the proposed approach. The other part does not meet the condition and then the integration is calculated by the Gaussian numerical integration. Fig. 9~12 present the relative error corresponding to this case. Second, the testing segment is parallel to the source segment. We fixed the testing point at $(0, 0.065, 0)$ [m], which is 0.02 m away from the vertex of the testing segment. The source segment is then divided into three parts. The middle part is calculated by the small argument approximation and the analytical formulations in the proposed approach, and the integration on other two parts is calculated by the Gaussian numerical integration. Fig. 13 shows results corresponding to this case. Two approaches including the proposed approach and the fully numerical integration are considered in our comparisons.

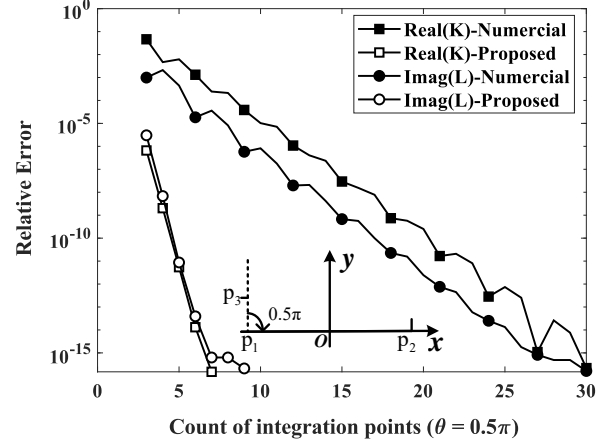


Fig. 10. Relative error obtained from the proposed approach and the fully numerical integration approach with $\theta = 0.5\pi$. The end points on source segment \mathbf{p}_1 , \mathbf{p}_2 are $(-0.065, 0, 0)$ [m] and $(0.065, 0, 0)$ [m], respectively. The testing point \mathbf{p}_3 is $(-0.065, 0.020, 0)$ [m] and 0.02 m away from \mathbf{p}_1 . The angle θ between the testing and source segments is 0.5π .

Two observations are made before we move to detailed numerical results:

- 1) After the small variable approximation is applied for the integral operator \mathcal{L} , its imaginary part is a linear function of $|\mathbf{r} - \mathbf{r}'|$ according to (48), which corresponds to the real part of \mathcal{L} as shown in (8). The integration calculated by the Gaussian integration approach is expected to be accurate enough. Therefore, it is of little significance to compare the real parts of results obtained from the two approaches. Similarly, the imaginary part of the operator \mathcal{K} is not considered in our comparisons.
- 2) The fully numerical integration approach suffers from the convergence issue when θ is small. For example, let's us consider $\theta = 0$. As the count of integration points increases, the testing and source points are approaching to each other and even coincide. The numerical integration shows extremely slow convergence and even totally does not convergent. Therefore, this scenario is not considered in our comparison. However, it should be noted that the proposed approach does not suffer from this issue and can still obtain accurate integration results.

Fig. 9~13 show the relative error obtained from the fully numerical integration approach and the proposed approach for two testing cases including the first one with $\theta = 0.1\pi, 0.5\pi, 0.75\pi, \pi$ and the second parallel one. The performance of the fully numerical integration approach changed a lot with different θ as shown in Fig. 9~12. It requires a large number of integration points, especially for small θ . As shown in Fig. 9, it needs over 100 integration points to obtain accurate enough results. However, as θ grows larger, the performance of the fully numerical approach in terms of the count of integration points becomes better. The reason is that \mathcal{L} and \mathcal{K} shows stronger nearly singular behaviors for smaller θ . However, for the proposed approach, the count of integration points is less than 10 points to reach the machine precision for all scenarios as shown in Fig. 9~13. Therefore,

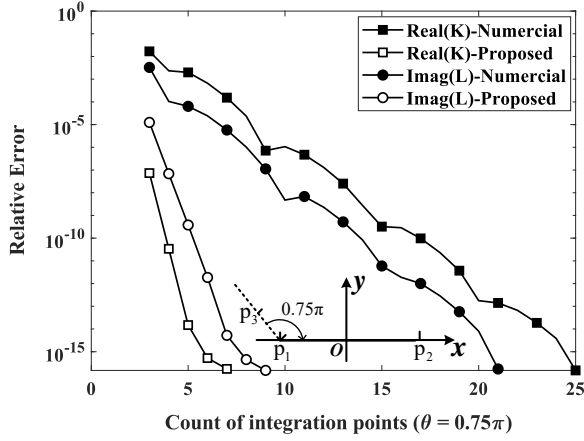


Fig. 11. Relative error obtained from the proposed approach and the fully numerical integration approach with $\theta = 0.75\pi$. The end points on source segment \mathbf{p}_1 , \mathbf{p}_2 are $(-0.065, 0, 0)$ [m] and $(0.065, 0, 0)$ [m], respectively. The testing point \mathbf{p}_3 is $(-0.079, 0.014, 0)$ [m] and 0.02 m away from \mathbf{p}_1 . The angle θ between the testing and source segments is 0.75π .

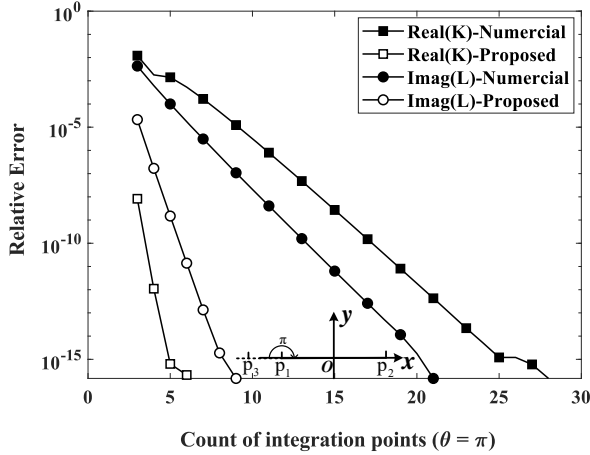


Fig. 12. Relative error obtained from the proposed approach and the fully numerical integration approach with $\theta = \pi$. The end points on source segment \mathbf{p}_1 , \mathbf{p}_2 are $(-0.065, 0, 0)$ [m] and $(0.065, 0, 0)$ [m], respectively. The testing point \mathbf{p}_3 is $(-0.085, 0, 0)$ [m] and 0.02 m away from \mathbf{p}_1 . The angle θ between the testing and source segments is π .

the proposed approach is quite accurate, efficient and robust to calculate the nearly singular and singular integrals in the proposed SS-SIE.

Another scattering example is carried out to further validate the accuracy of the proposed singularity cancellation approach. The radar cross section (RCS) of a homogeneous dielectric object with $\epsilon_r = 4$ is considered. Its cross section is an equilateral triangle with the side length of $\sqrt{3}$ m. The surrounding medium is air. A TE-polarized plane wave with the frequency of 300 MHz incidents from the x -axis. The length of all segments used to discretize the contour of the object is $\lambda/10$, where λ is the wavelength inside the penetrable object. In our comparisons, three approaches including the proposed singularity cancellation approach, the analytical approach [37] [38] and the fully numerical integration approach are used. For the analytical approach, only the self segments are treated to

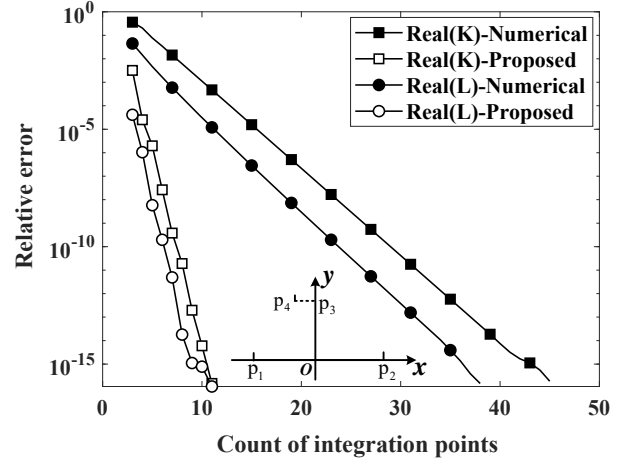


Fig. 13. Relative error obtained from the proposed approach and the fully numerical integration approach with $\theta = 0.1\pi$. The end points on source segment \mathbf{p}_1 , \mathbf{p}_2 are $(-0.065, 0, 0)$ [m] and $(0.065, 0, 0)$ [m], respectively. The testing point \mathbf{p}_3 is $(0, 0.065, 0)$ [m] and 0.02 m away from the end point \mathbf{p}_4 $(-0.02, 0.065, 0)$ [m]. The testing segment is parallel to the source segment.

be singular. Then, the Green's function and its gradient are approximated by (48) and (49) and analytical integration is applied. Other interactions are calculated through the Gaussian numerical integration. 14-points and 5-points Gaussian numerical integration for the source and testing line integration are used.

The reference RCS is calculated from the COMSOL with extremely fine mesh. As shown in Fig. 14, results obtained from the analytical approach can only get accurate RCS from 150° to 180° and show large errors in other regions. The reason is that numerical integration is not accurate enough to evaluate nearly singular integration. When the fully numerical approach is applied, it is interestingly found that results are much more accurate than those of the analytical approach and show good agreement in the whole range except from 20° to 50° . It maybe account for the reason that the numerical integration has almost uniform level of accuracy. When the proposed singularity cancellation approach is used, results show excellent agreement with the reference RCS. Through splitting the nearly singular and singular segments into the analytical and numerical integration parts and combining the numerical integration approach and integration cancellation approach, the singular and nearly singular integrals can be accurately calculated.

B. A Single Penetrable Object

In this subsection, two single penetrable objects, the equilateral triangle including non-smoothing boundaries and a dielectric cylinder with only smoothing boundaries, are considered. The radius of the dielectric cylinder is 1 m, the relative dielectric constant ϵ is 4. The background medium is air. The incident wave is a TE-wave from the x -axis with the frequency of 300 MHz. The length of all segments used to discretize the contour of the object is $\lambda/10$, where λ is the wavelength inside the penetrable object.

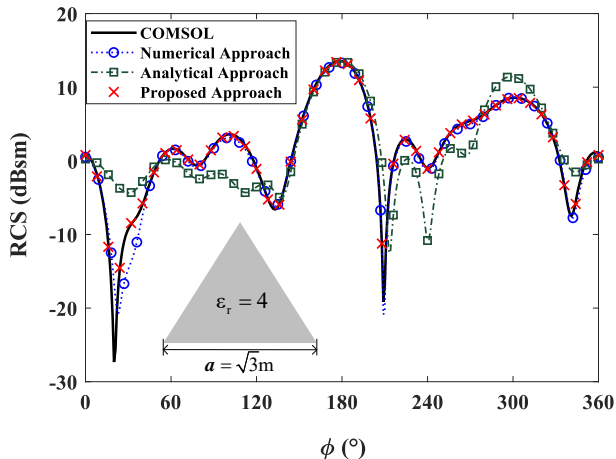


Fig. 14. RCS obtained from the proposed approach, the analytical approach and the COMSOL for a triangular dielectric object.

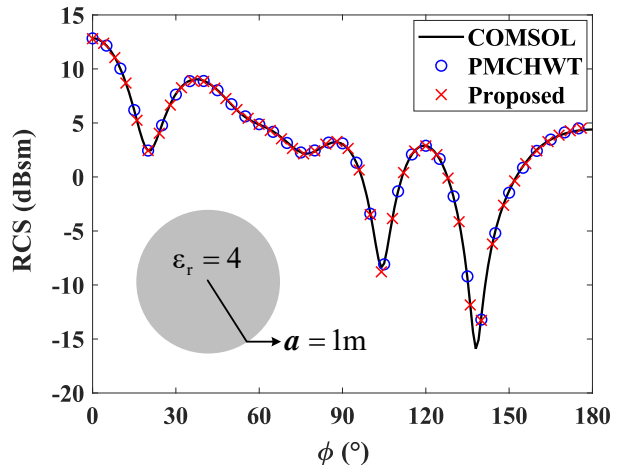


Fig. 15. RCS calculated by the proposed approach, the PMCHWT formulation and the Comsol for the dielectric cylinder.

The reference solution is obtained from the COMSOL with extremely fine mesh. The RCS of the triangle and cylinder dielectric objects are calculated as shown in Fig. 14, in which only results obtained from the COMSOL and the proposed approach are presented to demonstrate the effectiveness of the proposed singular cancellation approach, and Fig. 15 by the proposed approach, the COMSOL and the PMCHWT formulation, respectively. Results obtained from the three approaches are all in excellent agreement.

The overall count of unknowns for the PMCHWT formulation is 210 for the triangle object and 128 for the cylinder. However, only 105 and 64 is used for the proposed approach since only single current density is required. The condition numbers of the PMCHWT formulation and the proposed approach are 4, 711, 63.5 for the cylinder object and 96, 671, 391 for the triangle object, respectively. Therefore, the proposed SS-SIE shows better performance in terms of overall count of unknowns and condition number.

Fig. 16 and Fig. 17 show that the relative error with respect to averaged count of segments per wavelength (ACSPW) in the free space. The relative error in this subsection is defined as

$$RE = \frac{\sum_i \|\text{RCS}^{\text{cal}}(\phi_i) - \text{RCS}^{\text{ref}}(\phi_i)\|^2}{\sum_i \|\text{RCS}^{\text{ref}}(\phi_i)\|^2}, \quad (54)$$

where $\text{RCS}^{\text{cal}}(\phi_i)$ denotes results calculated from the proposed approach and $\text{RCS}^{\text{ref}}(\phi_i)$ is the reference solution obtained from the Comsol. As shown in Fig. 16 and Fig. 17, it can be found that the relative error fast exponentially decreases to the level of $10^{-3} \sim 10^{-4}$ as the ACSPW increases to 10. It is expected that more accurate results can be obtained for smoothing than non-smoothing objects. Then, its accuracy does not improve significantly when the mesh is further refined. This is because the linear basis function (10) is used in our current implementations.

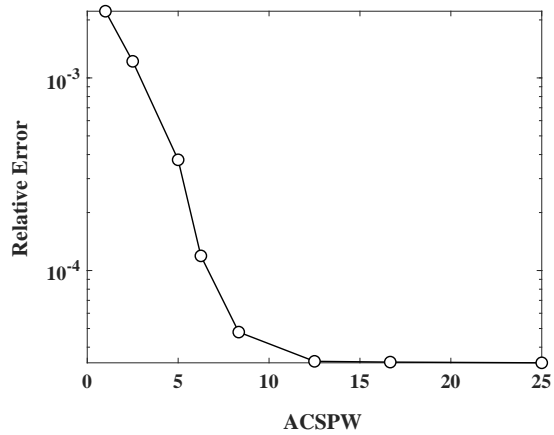


Fig. 16. Relative error with ACSPW for the dielectric cylinder.

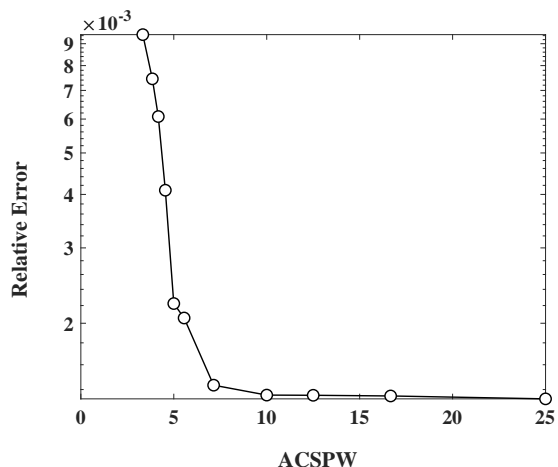


Fig. 17. Relative error with ACSPW for the dielectric triangular object.

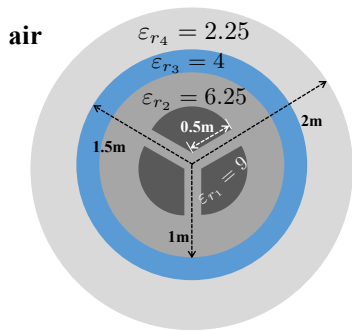


Fig. 18. The geometry configuration and constant parameters of the complex structure.

C. A Complex Structure

A complex structure with three dielectric 120-degree sector-shaped objects with $r_1 = 0.5\text{m}$ and $\epsilon_{r_1} = 9$ surrounded by three concentric cylinders is considered as shown in Fig. 18. The parameters of dielectric cylinders are $r_2 = 1\text{m}$, $r_3 = 1.5\text{m}$, $r_4 = 2\text{m}$ and the relative permittivity $\epsilon_{r_2} = 6.25$, $\epsilon_{r_3} = 4$, $\epsilon_{r_4} = 2.25$. The background medium is air. A plane wave with $f = 300\text{ MHz}$ incidents from the x -axis. The averaged length of segments used to discretize all the boundaries is $\lambda_0/20$, where λ_0 is the wavelength in the free space. It should be noted that this discretization corresponds to $\lambda/6.7$ inside the sector-shaped object with $\epsilon_{r_1} = 9$.

Fig. 18 shows that the RCS obtained from three approaches. It is easy to find that results obtained from the proposed approach are in excellent agreement with those from the COMSOL and the PMCHWT. Fig. 20 shows that the relative error with respect to ACSPW in the free space. It can be found that the relative error of the proposed approach decreases as the count of segments per wavelength increases. When the count is less than 16, the relative error exponentially converges. Then, after the count is larger than 20, the improvement of accuracy is less significant. When 20 segments per wavelength in the free space is used, which corresponds to $\lambda/6.7$ inside the sector-shaped object, the relative error almost reaches 10^{-3} . Therefore, the proposed approach shows quite good convergence property in terms of mesh size.

Table I shows the computational cost for the PMCHWT formulation and the proposed approach. For the PMCHWT formulation, it requires 1,048 unknowns to solve this problem. However, only 188 unknowns are required for the proposed approach. It can be found that the proposed approach only uses 5% memory of the PMCHWT formulation and shows significant memory saving. It should be noted that the vectorization is fully explored to speed up the in-house matlab codes. Therefore, more memory consumption are expected in our simulations. Since only the electric current density is enforced on the outermost boundary rather than both the electric and magnetic current densities on all the interfaces in the PMCHWT formulation, significant less unknowns are required. In this simulation, the proposed approach only needs 18% unknowns of the PMCHWT formulation. The overall computational time to solve this problem for the PMCHWT formulation is 15.34 seconds. Although overhead is required to

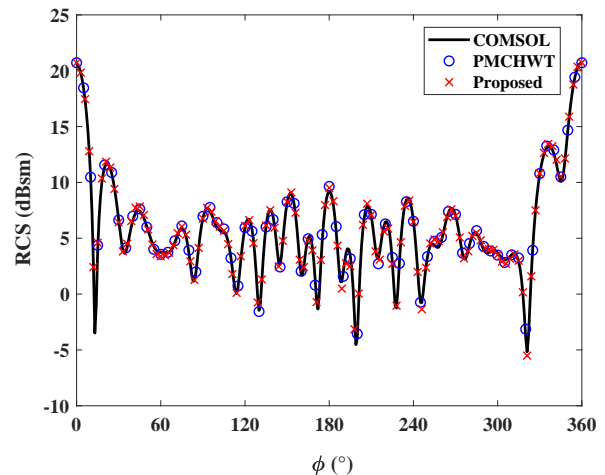


Fig. 19. RCS obtained from the proposed approach, the PMCHWT formulation, and the COMSOL.

derive the equivalent current density on the outermost boundary, only 10.65 seconds is needed for the proposed approach. In addition, the condition number of the final linear system for the PMCHWT formulation and the proposed approach is 41,095 and 213, respectively. The proposed approach shows much better conditioning since fine geometry details are only implicitly embedded in final system unlike in the PMCHWT formulation, where all these are directly coupled into the final system. Therefore, like formulations [23] [27], the proposed approach can significantly improve the conditioning and then the convergence properties.

TABLE I
COMPARISON OF COMPUTATIONAL COST FOR THE PMCHWT FORMULATION AND THE PROPOSED APPROACH

	PMCHWT	Proposed
Total Time [s]	15.34	10.65
Filling Time [s]	15.28	10.62
Solving Time [s]	0.06	0.03
Memory [MB]	2,900	150
Condition number	41,095	213
Overall Counts of Unknowns	1,048	188

D. An Array with 5×5 Single-layered Coated Dielectric Cylinders

In this subsection, an array with 5×5 single-layered coated dielectric cylinder is simulated as shown in Fig. 21. The inner objects are dielectric cylinders with $r_1 = 0.4\text{ m}$ and $\epsilon_{r_1} = 4$ surrounded by the coating dielectric medium with $r_2 = 0.5\text{m}$ and $\epsilon_{r_2} = 2.25$. The central distance between two adjacent cylinder elements is $d = 1.2\text{ m}$ and the background medium is air. The TE-wave with $f = 300\text{ MHz}$ incidents from the x -axis.

The RCS is computed from the proposed approach, the PMCHWT formulation and the COMSOL as shown in Fig.

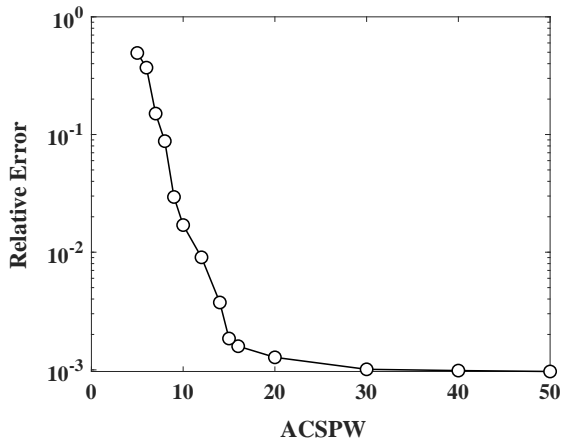


Fig. 20. Relative error with respect to ACSPW of the proposed approach in the free space.

TABLE II
COMPARISON OF COMPUTATIONAL COST FOR THE PMCHWT FORMULATION AND THE PROPOSED APPROACH

	PMCHWT	Proposed
Total Time [s]	1,371.3	804.8
Filling Time [s]	1,333	800
Solving Time [s]	37.9	4.8
Memory [MB]	4,200	400
Condition Number	328,890	4,008
Overall Counts of Unknowns	14,400	4,000

22 and $\lambda/20$ is selected for boundary discretization, where λ is the wavelength in the background medium. It can be found that results obtained from the proposed approach are in excellent agreement with the results from the PMCHWT formulation and the COMSOL.

Table II shows the computational cost of the PMCHWT formulation and the proposed approach. The count of unknowns from the PMCHWT formulation is 14,400. However, the proposed approach only requires only 4,000 to solve this problem. Since only the electric current density is required to enforce on the outermost boundaries, significant less count of unknowns is used in the proposed approach. For the memory consumption, 4,200 MB memory is used in the PMCHWT formulation. However, only 400 MB memory, 9.5% of the PMCHWT formulation, is used for the proposed method. The CPU time to fill coefficient matrix is 1,371.3s for the PMCHWT formulation and 804.8 for the proposed approach. Therefore, the CPU time is reduced by 42%. The computational time does not reduce linearly with the count of unknowns since overhead is required to construct the equivalent current density on the outermost boundaries. However, the saving in terms of memory and CPU time is still quite significant. It is found that the matrix condition number of the PMCHWT formulation is very large, which is 328,890 while the matrix condition number of the proposed method is only 4,008. It means

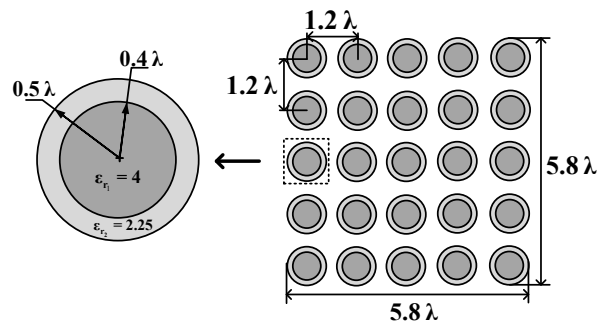


Fig. 21. An array with 5×5 single-layered coated dielectric cylinders.

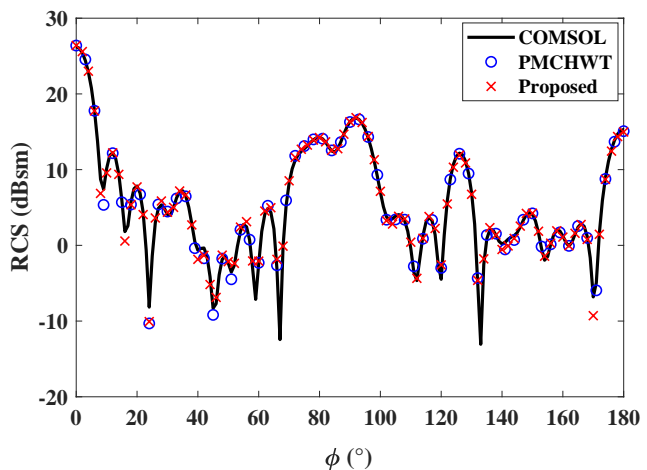


Fig. 22. RCS obtained from the proposed approach, the PMCHWT formulation, and the COMSOL.

that the proposed approach shows much better conditioning compared with the PMCHWT formulation.

VI. CONCLUSION

The surface equivalence theorem states that any enclosed surface with appropriate surface equivalent currents sources can generate an equivalent configuration with fields exactly the same as those in the original problems. In this paper, we fully explore this possibility in the method of moment implementations. A novel vector SS-SIE is proposed to solve TE scattering problems from objects embedded in multilayers. The results reported in this paper shows that the fully vector electromagnetic waves are also valid and greatly extended our previous researches in [34], which only works for the scalar TM-polarized electromagnetic problems.

The proposed approach in this paper only needs a single electric current density on the outermost boundary, which can be derived by recursively applying the surface equivalence theorem on each boundary from inner to exterior regions. Compared with the PMCHWT formulation, the proposed approach can significantly improve the efficiency in terms of overall count of unknowns, memory consumption, CPU time and condition number of the linear system. In addition, to accurately handling the nearly singular and singular integrals

in the proposed approach, an efficient singularity cancellation approach is proposed. Numerical results validate its accuracy, efficiency and convergence property of the singularity cancellation approach and the SS-SIE.

Extension of current work into three dimensional case to solve more practical engineering problems is in progress and we will report more results upon this topic in the future.

VII. APPENDIX

According to the definitions in Section IV, the following eight identities [41] [42] are used.

$$I_1 = \int_{l_i} \ln |\mathbf{R}| d\mathbf{r}' = l_+ \ln |\mathbf{R}_+| - l_- \ln |\mathbf{R}_-| + |\mathbf{p}_0| \left(\tan^{-1} \frac{l_+}{|\mathbf{p}_0|} - \tan^{-1} \frac{l_-}{|\mathbf{p}_0|} \right) - (l_+ - l_-), \quad (55)$$

$$I_2 = \int_{l_i} \vec{l} \cdot \ln |\mathbf{R}| d\mathbf{r}' = \frac{\vec{\tau}}{2} \cdot \left\{ -\frac{1}{2} [(l_+)^2 - (l_-)^2] + |\mathbf{R}_+|^2 \ln |\mathbf{R}_+| - |\mathbf{R}_-|^2 \ln |\mathbf{R}_-| \right\}, \quad (56)$$

$$I_3 = \int_{l_i} \frac{1}{|\mathbf{R}|^2} d\mathbf{r}' = \frac{1}{|\mathbf{p}_0|} \left(\tan^{-1} \frac{l_+}{|\mathbf{p}_0|} - \tan^{-1} \frac{l_-}{|\mathbf{p}_0|} \right), \quad (57)$$

$$I_4 = \int_{l_i} \frac{\vec{l}}{|\mathbf{R}|^2} d\mathbf{r}' = \vec{\tau} \cdot (\ln |\mathbf{R}_+| - \ln |\mathbf{R}_-|), \quad (58)$$

$$I_5 = \int_{l_i} \frac{\vec{l} \cdot \vec{l}}{|\mathbf{R}|^2} d\mathbf{r}' = (l_+ - l_-) - |\mathbf{p}_0|^2 \cdot I_3, \quad (59)$$

$$I_6 = \int_{l_i} 1 d\mathbf{r}' = l_+ - l_-, \quad (60)$$

$$I_7 = \int_{l_i} \vec{l} d\mathbf{r}' = \frac{\vec{\tau}}{2} [(l_+)^2 - (l_-)^2], \quad (61)$$

$$I_8 = \int_{l_i} \vec{l} \cdot \vec{l} d\mathbf{r}' = \frac{1}{3} [(l_+)^3 - (l_-)^3]. \quad (62)$$

Based on the above eight integrals, we can accurately calculate the nearly singular and singular integrals in (8) and (9) in the proposed SS-SIE.

REFERENCES

- [1] U. R. Patel, B. Gustavsen, and P. Triverio, "An equivalent surface current approach for the computation of the series impedance of power cables with inclusion of skin and proximity effects," *IEEE Trans. Power Del.*, vol. 28, pp. 2474-2482, 2013.
- [2] A. Siripuram and V. Jandhyala, "Surface interaction matrices for boundary integral analysis of lossy transmission lines," *IEEE Trans. Microw. Theory Tech.*, vol. 57, no. 2, pp. 347-382, Feb. 2009.
- [3] W. Gibson, *The Method of Moments in Electromagnetics*. CRC press, 2015.
- [4] A. Taflov and S. Hagness, *Computational Electrodynamics: the Finite-Difference Time-Domain Method*. Artech house, 2005.
- [5] J. Jin, *The finite element method in electromagnetics*. New York, NY, USA: Wiley, 2015.
- [6] A. J. Poggio and E. K. Miller, "Integral equation solutions of three-dimensional scattering problems," in *Computer Techniques for Electromagnetics*. R. Mittra, Ed. Oxford, U.K.: Pergamon, 1973.
- [7] P. Ylä-Oijala, M. Taskiran, and S. Järvenpää, "Surface integral equation formulations for solving electromagnetic scattering problems with iterative methods," *Radio Sci.*, vol. 40, no. 6, pp. 119, Dec. 2005.
- [8] C. Müller, *Foundations of the Mathematical Theory of Electromagnetic Waves*. New York: Springer-Verlag, 1969. vol. 61, no. 1, pp. 341350, Jan. 2013.
- [9] J. Hu, R. Zhao, Y. Zhang, M. Jiang and Z. Nie, "Fast solving EM scattering from penetrable objects with non-conformal multiple-traces PMCHWT equations," in *IEEE Int. Conf. Ubiquitous Wirel. Broadband (ICUWB)*, Nanjing, 2016, pp. 1-3.
- [10] T. Tanaka, Y. Nishioka, Y. Inasawa and H. Miyashita, "Verification of the PMCHWT-CBFM for scattering analysis of a microstrip array antenna," in *Eur. Conf. Antennas Propag. (EuCAP)*, The Hague, 2014, pp. 3232-3236.
- [11] A. Menshov, V. Okhmatovski, "New single-source surface integral equations for scattering on penetrable cylinders and current flow modeling in 2-D conductors," *IEEE Trans. Microw. Theory Tech.*, vol. 61, no. 1, pp. 341-350, Jan. 2013.
- [12] Y. Shi, C. H. Liang, "An efficient single-source integral equation solution to EM scattering from a coated conductor," *IEEE Antennas Wirel. Propag. Lett.*, vol. 14, pp. 547-550, Nov. 2014.
- [13] F. S. H. Lori, M. S. Hosen, and V. Okhmatovski, "Higher order method of moments solution of the new vector single-source surface integral equation for 2D TE scattering by dielectric objects," in *IEEE MTT-S Int. Conf. Numer. Electromagn. Multiphysics Model. Optim. RF, Microw., Terahertz Appl. (NEMO)*, Seville, 2017, pp. 161-163.
- [14] L. Hosseini, A. Menshov, R. Gholami, J. Mojolagbe, and V. Okhmatovski, "Novel single-source surface integral equation for scattering problems by 3-D dielectric objects," *IEEE Trans. Antennas Propag.*, vol. 66, no. 2, pp. 797-807, Dec. 2017.
- [15] D. R. Swatek, I. R. Ciric, "Single source integral equation for wave scattering by multiply-connected dielectric cylinders," *IEEE Trans. Magn.*, vol. 32, no. 3, pp. 878-881, May. 1996.
- [16] Z. G. Qian, W. C. Chew, and R. Suaya, "Generalized impedance boundary condition for conductor modeling in surface integral equation," *IEEE Trans. Microw. Theory Tech.*, vol. 55, pp. 2354-2364, Nov. 2007.
- [17] D. De Zutter, L. Knockaert, "Skin effect modeling based on a differential surface admittance operator," *IEEE Trans. Microw. Theory Tech.*, vol. 53, no. 8, pp. 2526-2538, Aug. 2005.
- [18] U. R. Patel and P. Triverio, "Skin effect modeling in conductors of arbitrary shape through a surface admittance operator and the contour integral method," *IEEE Trans. Microw. Theory Tech.*, vol. 64, no. 9, pp. 2708-2717, Aug. 2016.
- [19] U. R. Patel, B. Gustavsen, and P. Triverio, "Proximity-aware calculation of cable series impedance for systems of solid and hollow conductors," *IEEE Trans. Power Del.*, vol. 29, no. 5, pp. 2101-2109, Oct. 2014.
- [20] P. Utkarsh, and P. Triverio, "MoM-SO: a complete method for computing the impedance of cable systems including skin, proximity, and ground return effects," *IEEE Trans. Power Del.*, vol. 30, no. 5, pp. 2110-2118, Oct. 2015.
- [21] H. Martijn, D. D. Zutter, D. V. Ginste, "A fully 3-D BIE evaluation of the resistance and inductance of on-board and on-chip interconnects," in *IEEE Workshop Signal Power Integrity (SPI - Proc.)*, Brest, 2018, pp. 1-4.
- [22] U. R. Patel, P. Triverio, and S. V. Hum, "A novel single-source surface integral method to compute scattering from dielectric objects," *IEEE Antennas Wirel. Propag. Lett.*, vol. 16, pp. 1715-1718, Feb. 2017.
- [23] U. R. Patel, P. Triverio, and S. V. Hum, "A macromodeling approach to efficiently compute scattering from large arrays of complex scatterers," *IEEE Trans. Antennas Propag.*, vol. 66, no. 11, pp. 6158-6169, Nov. 2018.
- [24] H. Martijn, M. Gossye, D. D. Zutter, and D. V. Ginste, "A 3-D differential surface admittance operator for lossy dipole antenna analysis," *IEEE Antennas Wirel. Propag. Lett.*, vol. 16, pp. 1052-1055, 2017.
- [25] H. Martijn, D. D. Zutter, and D. V. Ginste, "Broadband 3-D boundary integral equation characterization of composite conductors," in *IEEE Conf. Electr. Perform. Electron. Packag. Syst. (EPEPS)*, Montreal, 2019, pp. 1-3.
- [26] H. Martijn, K. Y. Kapsuz, X. Sun, G. V. D. Plas, E. Beyne, D. D. Zutter, and D. V. Ginste, "Entire domain basis function expansion of the differential surface admittance for efficient broadband characterization of lossy interconnects," *IEEE Trans. Microw. Theory Tech.*, vol. 68, pp. 1217-1233, Apr. 2020.
- [27] M. K. Li, W. C. Chew, "Wave-field interaction with complex structures using equivalence principle algorithm," *IEEE Trans. Antennas Propag.*, vol. 55, no. 1, pp. 130-138, Jan. 2007.
- [28] M. K. Li and W. C. Chew, "Multiscale simulation of complex structures using equivalence principle algorithm with high-order field point sampling scheme," *IEEE Trans. Antennas Propag.*, vol. 56, no. 8, pp. 2389-2397, Aug. 2008.
- [29] F. G. Hu and J. M. Song, "Integral equation analysis of scattering from multilayered periodic array using equivalence principle and connection

- scheme," *IEEE Trans. Antennas Propag.*, vol. 58, no. 3, pp. 848-856, Mar. 2010.
- [30] C. Balanis, *Antenna Theory: Analysis and Design*. 3rd ed. Wiley, 2005.
- [31] G. W. Hanson, A. B. Yakovlev, *Operator Theory for Electromagnetics*. Springer, 2002.
- [32] M. A. Jensen, J. D. Freeze, "A recursive green's function method for boundary integral analysis of inhomogeneous domains," *IEEE Trans. Antennas Propag.*, vol. 46, pp. 1810-1816, Dec. 1998.
- [33] X. C. Zhou, Z. K. Zhu, S. C. Yang, and D. L. Su, "A novel single source surface integral equation for electromagnetic analysis by multilayer embedded objects," in *Int. Appl. Comput. Electromagn. Soc. Symp.-China (ACES)*, Nanjing, 2019.
- [34] X. C. Zhou, Z. K. Zhu, S. C. Yang, and D. L. Su, "Towards a unified approach to electromagnetic analysis by multilayer embedded objects," arXiv preprint, arXiv:1909.01854.
- [35] Z. K. Zhu, X. C. Zhou, J. Wang, and S. C. Yang, "Single-source SIE for TE electromagnetic analysis of penetrable objects," in *IEEE Int. Symp. Antennas Propag. USNC-URSI Radio Sci. Meet. (APSURSI)*, Montrealin, 2020, in press.
- [36] . Ergl, L. Grel, "The use of curl-conforming basis functions for the magnetic-field integral equation," *IEEE Trans. Antennas Propag.*, vol. 54, pp. 1917-1926, July. 2006.
- [37] R. F. Harrington, *Field Computation by Moment Methods*. New York: Macmillan, 1968.
- [38] Y. Liu, H. Z. Yang, "A hierarchicalbutterflyLU preconditioner for two-dimensional electromagnetic scattering problems involving open surfaces," *J. Comput. Phys.*, vol. 401, Jan. 2020.
- [39] Y. F. Jing, T. Z. Huang, Y. Duan, "A novel integration method for weak singularity arising in two-dimensional scattering problems," *IEEE Trans. Antennas Propag.*, vol. 58, pp. 2725-2731, Aug. 2010.
- [40] F. S. H. Lori, A. Menshov, V. Okhmatovski, "New vector single-source surface integral equation for scattering problems on dielectric objects in 2D," *IEEE Trans. Antennas Propag.*, vol. 65, pp. 3794-3799, July. 2017.
- [41] D. R. Wilton, S. M. Rao, A. W. Glisson, "Potential integrals for uniform and linear sources distribution on polygonal and polyhedral domains," *IEEE Trans. Antennas Propag.*, vol. AP-32, pp. 276-281, Mar. 1984.
- [42] J. Stewart, *Calculus*, Brooks Cole, 2007.